Transition metal-doped nickel phosphide nanoparticles as electro- and photocatalysts for hydrogen generation reactions

Ho-Wing Man[a], Chui-Shan Tsang[a], Molly Meng-Jung Li[b], Jiaying Mo[b], Bolong Huang[a], Lawrence Yoon Suk Lee[a,*], Yun-chung Leung[a], Kwok-Yin Wong[a], Shik Chi Edman Tsang[a,b,*]

[a] Department of Applied Biology and Chemical Technology and the State Key Laboratory of Chemical Biology and Drug Discovery, The Hong Kong Polytechnic University, Hung Hom, Kowloon, Hong Kong
[b] Department of Chemistry, University of Oxford, Oxford, OX1 3QR, UK

ARTICLE INFO

ABSTRACT

Transition metal-doped nickel phosphide nanoparticles with metallic properties are prepared by a simple and facile wet-chemical method. It is shown for the first time that these transition metals: iron, cobalt, manganese, and molybdenum, can atomically substitute nickel in the parent *hcp* phosphide lattice as a single phase without significant change in its metallic structure and morphology. They are employed as electro- and photocatalysts for hydrogen evolution reaction, which show highly tunable activities dependent on electron filling of their metallic bands and H coverage according to our experimental and theoretical rationalizations. Molybdenum-doped nickel phosphide nanoparticle with lower H coverage exhibits the best hydrogen evolution performance in electrocatalytic hydrogen evolution reaction, which also shows excellent photocatalytic hydrogen production with organic photosensitizer. In addition, cobalt-doped nickel phosphide nanoparticle with higher H coverage with aqueous photosensitizer gives more superior hydrogen evolution rate.

1. Introduction

With the continuous and exponential increase in global energy demand and severe environmental issues, sustainable and renewable energy sources are required to replace fossil fuels. Hydrogen fuel is one of the good candidates because of its environmental friendly nature and high energy output through combustion [1–3]. One of the most promising ways to produce hydrogen is through hydrogen evolution reaction (HER), by either electro- or photocatalysis. In electrocatalytic HER, platinum group metals (PGMs), such as platinum, are found to be the most active HER electrocatalysts [4]. In addition to electrocatalytic HER, PGMs are also employed in photoelectrochemical HER [5]. However, PGMs are scarce and expensive to be used. Alternatives such as MoS_2 and TiO_2, composed of cheaper and more earth-abundant elements, show promising catalytic activities in either electro- or photocatalytic HER [6,7].

Recently, transition metal phosphides (TMPs) with comparable metallic properties to carry out reversible dissociation or association of H to H_2 have drawn much attention as potential HER catalysts. Particularly for nickel phosphide, Liu and Rodriguez have conducted DFT calculations on estimating the Gibbs free energy of hydrogen

adsorption (ΔG_H), a descriptor for HER, on $Ni_2P(001)$ surface [8]. The calculation suggested that $Ni_2P(001)$ surface could even show a higher activity under some specific conditions than Pt on a thermodynamic basis. After that, Ni_2P nanoparticle was experimentally demonstrated to display excellent electrocatalytic HER activity under acidic conditions [9]. Further improvements were made on nickel phosphide through the preparation of different crystal phases [10–12] and the incorporation of carbonaceous materials [13–15]. Most recently, it has been also demonstrated that nickel phosphide can be used as an active component in HER photocatalysis, when it is mixed with semiconductor phases, including CdS and g-C_3N_4 [16–18]. Electrons are thought to be transferred from the photo-excited conduction bands of semiconductors to Ni_2P, which eventually lead to hydrogen production from the phosphide surface. In order to get an optimal H_2 production rate, tuning appropriate metal-H bond strength is important to facilitate H^+ adsorption and reduction (Volmer step) and surface combination and desorption of dihydrogen (Tafel step) [19,20]. The incorporation of another metal surface of different metal-H bond strength to form a composite is a common strategy, which speeds up both Vomer and Tafel steps. This approach has been widely studied on metals and metal oxide composites in both theoretical and experimental aspects [21–24].

Attempts have been made on nickel phosphide-based systems where other transition metals are incorporated with the nickel phosphide as separated phases in the composites [25–27]. In particular, nickel and cobalt phosphides are prepared with g-C$_3$N$_4$ to form a composite and employed as a HER photocatalyst, achieving an excellent hydrogen production rate [28]. Herein, we report that transition metals, including iron, cobalt, manganese, and molybdenum, are successfully incorporated into nickel phosphide crystal lattice as a *single phase* to form transition metal-doped nickel phosphide nanoparticles through simple and facile wet-chemical method. The as-prepared transition metal-doped nickel phosphide (NiMP) nanoparticles are shown to have improvements both in electro-and photocatalytic HER over pristine nickel phosphide (Ni$_2$P) nanoparticle.

2. Experimental section

2.1. Synthesis of pristine and metal-doped nickel phosphide nanoparticles

Typically, 1 mmol of nickel(II) acetate tetrahydrate was mixed in 5 mL of oleylamine in a 100 mL three-necked round-bottomed flask. The mixture was put under vacuum to remove adventitious oxygen and moisture. 11.2 mmol of trioctylphosphine (TOP) and equimolar of trioctylphosphine oxide (TOPO) were added to the flask sequentially. The reaction mixture was heated at 300 °C for 2 h under N$_2$ protection. After 2 h reaction, the reaction mixture was cooled down naturally by removal of heat source. 30 mL absolute ethanol was added, and precipitate was collected by centrifugation at 9000 rpm for 5 min. Supernatant was discarded and precipitate was purified by redispersion/precipitation process using chloroform and ethanol. The process was repeated for three times and purified product was dried and kept under vacuum. The synthetic procedures of metal-doped nickel phosphide nanoparticles were similar to the pristine one. 0.5 mmol of iron(II) acetate, manganese(III) acetate dihydrate, and cobalt(II) acetate were added with 0.5 mmol nickel(II) acetate tetrahydrate for the preparation of iron-, manganese-, and cobalt-doped nickel phosphide nanoparticles. 0.25 mmol of molybdenum acetate dimer was used to maintain metal ion concentration for preparing molybdenum-doped nickel phosphide nanoparticle.

2.2. Characterization

X-Ray powder diffraction pattern was obtained using Rigaku SmartLab with scan rate of 1° min^{-1}. Powder sample was placed on a silicon wafer and pressed using a glass slide. Diffraction pattern from 2θ = 35° to 60° was obtained for pristine and various metal-doped nickel phosphide nanoparticles. As-prepared powder samples were dispersed and sonicated in chloroform to obtain well-dispersed suspension. 20–40 μL of suspension was added on a 400-mesh copper grid with holely carbon coating and dried naturally. Images from transmission electron microscopy were obtained using a scanning transmission electron microscope (JOEL JEM-2100F). Selected area electron diffraction (SAED) and energy-dispersive X-ray spectroscopy (EDX) were carried out in tandem in transmission electron microscopy. X-Ray photoelectron spectra of pristine and various metal-doped nickel phosphide nanoparticles were obtained using X-Ray photoelectron spectrophotometer (ESCALAB 250 Xi) with approximately 20 mg of powder sample. Calibration was done using binding energy of C 1s energy level at 284.8 eV as reference. Local structures surrounding Ni and Fe atoms were probed by using extended X-ray absorption fine structure (EXAFS) technique in B18 Diamond light source. A Si(111) Double Crystal Monochromator (DCM) was used to scan the photon energy. The energy resolution (ΔE/E) for the incident X-ray photons was estimated to be 2 × 10^{-4}. Transmission mode was adopted for Ni K-edge and Fe K-edge EXAFS measurements. To ascertain the reproducibility of experimental data, at least two scan sets were collected and compared for each sample. The EXAFS data analysis was performed using IFEFFIT 1 with Horae packages 2 (Athena and Artemes). The spectra were calibrated with Ni and Fe metal foils as the references to avoid energy shifts of the samples. The amplitude reduction factors were obtained from EXAFS data analysis of the references, which were used as the fixed input parameters in the data fitting to allow the refinement in the coordination number of the absorption element. In this work, the first shell data analyses under the assumption of single scattering were performed with the errors estimated by R-factor.

2.3. Electrochemical measurement

To prepare the working electrode, catalyst ink was prepared by dissolving 2.5 mg metal-doped nickel phosphide nanoparticles in a solution containing 460 μL ethanol-water mixture (3:7) and 40 μL 5 wt.% Nafion solution. Working electrode was prepared by drop-casting 10 μL of catalyst ink on a glassy carbon electrode (GCE, d = 3 mm, surface area = 0.07 cm^2). The catalyst ink was dried naturally. Electrochemical measurements were performed using a CHI potentiostat (CHI1030A). Electrocatalytic hydrogen evolution reaction was conducted in a typical three-electrode system, using Pt mesh and saturated calomel electrode (SCE) as the counter and reference electrode, respectively, in 1 M potassium hydroxide solution (pH = 13). The electrolyte solution was purged with Ar for 30 min before measurements to get rid of dissolved oxygen and provide inert atmosphere. Linear sweep voltammetry (LSV) was carried out at room temperature in a potential range from −1 to −1.9 V with a scan rate of 5 mV s^{-1}. The potential measurements against saturated calomel electrode (SCE) were converted with respect to the reversible hydrogen electrode (RHE) according to the following equation [29]:

$$E_{RHE} = E_{SCE} + 0.244 + 0.0592(pH)$$

2.4. Photocatalytic testing

5 mg of catalyst and 64 mg of dye were mixed in a 55 mL quartz flask containing 20 mL TEOA-DMF (15% v/v) solution. The solution was sonicated for 15 min to achieve a good dispersion and degassed with Ar for 15 min afterwards. The flask was illuminated with a 450 W Xe lamp equipped with an AM1.5 filter (Newport OPSA1000) for 2 h. Gas generated in the headspace (250 mL) was withdrawn using an airtight syringe and analyzed using a gas chromatograph equipped with thermal conductivity detector (GC-TCD, Agilent 7890B) and ValcoPLOT Molesieve 5Å PLOT column (CFS-X3053-500). The amount of H$_2$ generated was calculated based on the calibration curve. H$_2$ production rate was calculated based on the metal content of the catalyst determined by energy dispersive X-ray spectroscopy.

2.5. Photostability test

The stability against photo-corrosion was tested out using NiMoP nanoparticle. The preparation of solution and analysis of hydrogen produced by photocatalysis are the same as the previous descriptions. The duration of one photocatalysis run was set to 5 h and five consecutive runs were conducted. After each run, NiMoP nanoparticle was collected by centrifugation and re-suspended in a fresh DMF solution with [Ru(bpy)$_3$](ClO$_4$)$_2$ and triethanolamine.

3. Results and discussion

To synthesize transition metal-doped nickel phosphide (NiMP) nanoparticles, Ni(OAc)$_2$·4H$_2$O and M(OAc)$_x$ were heated in the presence of oleylamine, trioctylphosphine (TOP), and trioctylphosphine oxide (TOPO) at 300 °C for 2 h. Fig. 1 shows the X-ray diffraction (XRD) patterns of pristine nickel phosphide (Ni$_2$P) and all NiMP nanoparticles which are in good match to the reported Ni$_2$P crystal structure (PDF#-
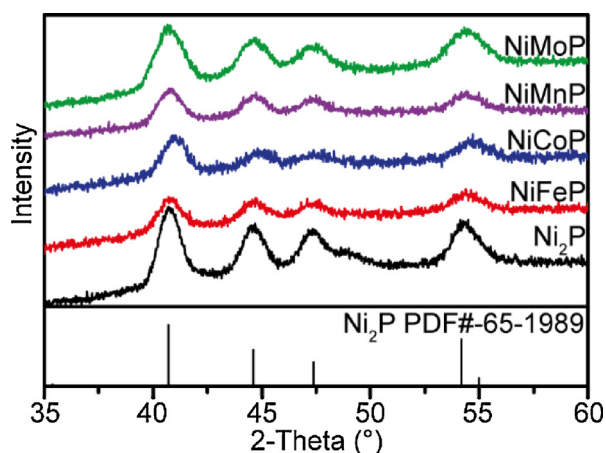
Fig. 1. XRD patterns of Ni$_2$P and various NiMP nanoparticles.

65-1989).

TEM images show the formation of all spherical nanoparticles with an average diameter of approximately 7 nm, except for NiMoP nanoparticles of having 5.3 ± 1 nm (Fig. 2). Electron diffraction patterns of all samples tested are almost identical, consisting four rings of diffraction. The predominant (111) lattice fringe shows a *d*-spacing of 0.22 nm. The selected area electron diffraction (SAED) pattern shows the rings of diffraction, where the innermost ring is indexed as (111) lattice plane and the outermost ring corresponds to (300) lattice plane. The measurements of *d*-spacing and electron diffraction pattern are in good agreements with XRD patterns mentioned previously. The elemental composition is determined by EDX (**Figs. S1–S5**, **Table S1** in Supplementary Information). In particular, the normalized ratio of elements in NiFeP nanoparticle (nickel-to-iron-to-phosphorus) is 1:0.1:0.7. An overall 6% of iron is successfully doped into the nickel phosphide crystal lattice.

X-ray photoelectron spectroscopy (XPS) shows that the as-synthesized NiMP nanoparticles display metallic properties where the binding energies of different metal-phosphorus bonds are similar to metals at Fermi state. XPS spectra and detailed peak deconvolutions are shown in
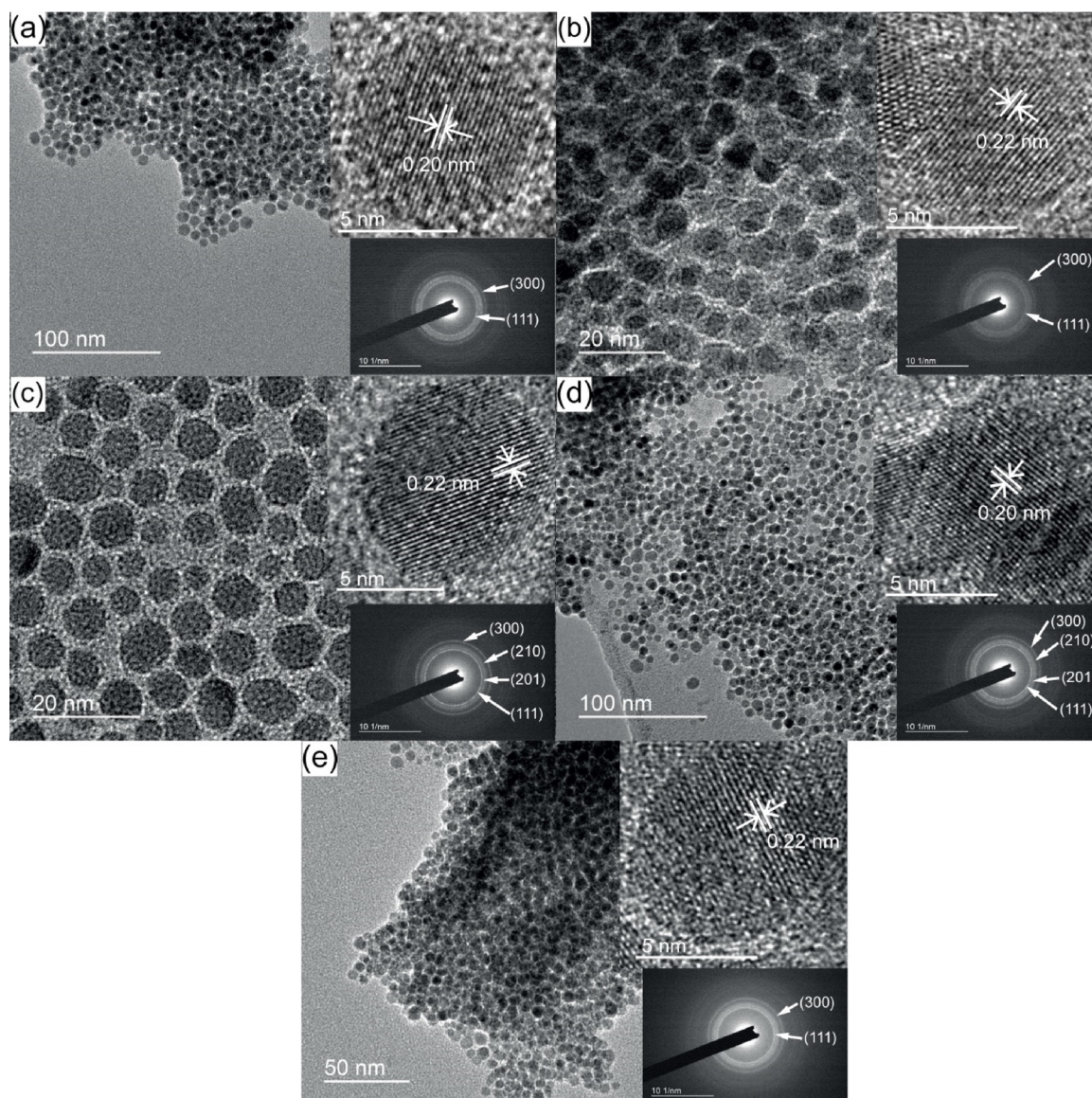

Fig. 2. TEM images of inset. (a) Ni$_2$P, (b) NiFeP, (c) NiCoP, (d) NiMnP, and (e) NiMoP nanoparticles. HR-TEM images and selected area electron diffraction patterns are shown as inset.

Table 1
EXAFS of Ni_2P and NiFeP nanoparticles.

	Bond	Enot[a]	Coordination number	ss	Bond length (Å)	R-factor
Ni_2P	Ni−P	2.7	2.9(2)	0.008(1)	2.25(1)	0.6%
	Ni−Ni		3.3(3)	0.008(1)	2.59(1)	
NiFeP	Ni−P	4.3	2.3(3)	0.008(2)	2.24(1)	1.3%
	Ni−Ni		2.5(3)	0.006(1)	2.59(1)	
	Fe−P	5.5	3.7(3)	0.007(1)	2.21(1)	2.0%
	Fe−Ni		3.6(3)	0.005(1)	2.63(1)	

[a] Enot is the energy difference between the absorption energies in experimental and calculated values.

Supplementary Information (**Figs. S6–S10**). In addition to the above characterization, typical extended X-ray absorption fine structure (EXAFS) measurement was carried out on Ni_2P and NiFeP nanoparticles to investigate the local bonding environments of metals (Table 1 and **Figs. S11–S13**). Ni−P and Ni−Ni bonds in NiFeP nanoparticle are determined as 2.24 and 2.59 Å, respectively, which match with those in Ni_2P nanoparticle in *hcp* structure as shown in SI (2.25 and 2.59 Å for Ni−P and Ni−Ni bonds, respectively). Meanwhile, the fitted Fe-Ni and Fe−P bonds are very similar to Ni−P and Ni−Ni as 2.63 and 2.21 Å, respectively. The bond lengths in iron-doped and pristine nickel phosphide nanoparticles are comparable which shows the incorporation of iron in nickel phosphide crystal lattice does not induce significant changes in bond strengths of existing Ni−Ni and Ni−P bonds. Typical coordination numbers in Ni−Ni and Ni−P for Ni_2P are 3 for both, which are close to our fittings as shown in Table 1, having coordination numbers for Ni−Ni and Ni−P as 3.3 and 2.9, respectively [30]. There is, however, a decrease in the coordination numbers when Fe is introduced into the crystal lattice. The coordination numbers for Ni−Ni and Ni−P in NiFeP nanoparticles are 2.5 and 2.3, respectively, whereas those for Fe−Ni and Fe−P are determined to be 3.6 and 3.7, respectively. The decreased coordination numbers of Ni−Ni and Ni−P indicate the successful substitution of Ni with Fe. In addition, the change in coordination number does not reveal a perfect substitution since there is a degree of mismatch between the added coordination numbers of Ni−P and Fe−P in NiFeP nanoparticle and that of Ni−P in Ni_2P nanoparticle. But, the basic *hcp* structure is clearly maintained. From the above control experiments for NiFeP nanoparticle synthesis, it was confirmed that iron present in the reaction environment can be incorporated into nickel phosphide crystal lattice without making much significant effect on the morphology, crystal structure, and bonding environment of the resulting nanoparticles despite the large degree of Fe incorporation.

4. Electro- and photocatalytic performances

Working electrodes of our samples were prepared by drop-casting the corresponding catalyst ink on glassy carbon electrodes, with a loading of $0.7\,mg\,cm^{-2}$. Linear sweep voltammograms were obtained from 0 to $-0.8\,V$ (*vs.* RHE, unless stated otherwise) in 1 M potassium hydroxide solution (Fig. 3a). The overpotential of Ni_2P is determined as 0.71 V to reach a low current density of $10\,mA\,cm^{-2}$ (low H-coverage). For all NiMP nanoparticles prepared, cathodic shifts are seen on all the corresponding polarization plots, indicating that enhancement in HER catalytic performance. The overpotential at $10\,mA\,cm^{-2}$ for Mo, Mn, Fe, Co-doped, and pristine nickel phosphide (abbreviated as NiMoP, NiMnP, NiFeP, NiCoP, Ni_2P) nanoparticles are 0.4, 0.49, 0.69, 0.53, and 0.71 V, respectively. This order almost inversely follows their number of electrons in d orbital, ($Mo(d^6)$; $Mn(d^7)$; $Fe(d^8)$; $Co(d^9)$ and $Ni(d^{10})$), with exception of the relative positions of Fe and Co. This reflects the d^8 electron contribution of Ni to the metallic bands is perhaps too much above the optimal chemisorption of H^+ and reduction to lead to lower HER activity. Substitution of Ni with elements of lower number of d-electrons at 1:1 of Ni:M ratio appears to shift towards the optimal value for the HER [31,32]. However, the precise order of metal dopers is dependent on the H coverage (where their current density values are compared) in some cases, especially for Co which is highly sensitive to the coverage and may switch with Fe in their positions, as shown later (Fig. 9). In addition, all the samples tested yielded relatively high Tafel slopes shown in Fig. 3b ($> 100\,mV\,dec^{-1}$). These slopes indicate the rate determining step is associated with Volmer step where the adsorption of hydrogen on catalyst surface at low H coverage is involved. The result is consistent with the DFT calculations by Liu and Rodriguez [8] in which the hydrophobic Ni_2P nanoparticle has a positive value of Gibbs free energy of hydrogen adsorption ($\Delta G_H = 0.31\,eV$). The exchange current densities of Ni_2P and various NiMP nanoparticles are tabulated in Table 2. NiMoP nanoparticle shows the lowest overpotential and one of the highest exchange current densities (high degree of mobile electrons), giving the best overall HER activity among the samples tested. Doping of Mo enhances the HER catalytic property from delocalization of 4d-electrons [31,32]. Mo, the most d-electron deficient transition metal among samples tested, as well as with the more outstretching nature of 4d compared to 3d orbital, leads to the largest degree of d-electron delocalization. However, compared to Pt, the best benchmark hydrogen-evolving electrocatalyst (a Tafel slope of $61\,mV\,dec^{-1}$), NiMoP nanoparticle shows moderate electrocatalytic activity in alkaline medium.

The positions of valence bands of different metallic NiMP nanoparticles were determined by valence band-X ray photoelectron spectroscopy (VB-XPS) and are shown in Fig. 4. Typical nature of metallic bands of these structures between 0 to $-10\,eV$ with the maxima value lower than the thermodynamic proton reduction potential (0.00 eV) indicate that activation energy must be required for the hydrogen production.

Apart from using electromotive force as excitation source, NiMP nanoparticle is also employed for HER by photoexcitation. Photocatalytic HER was carried out in the presence of photosensitizer,
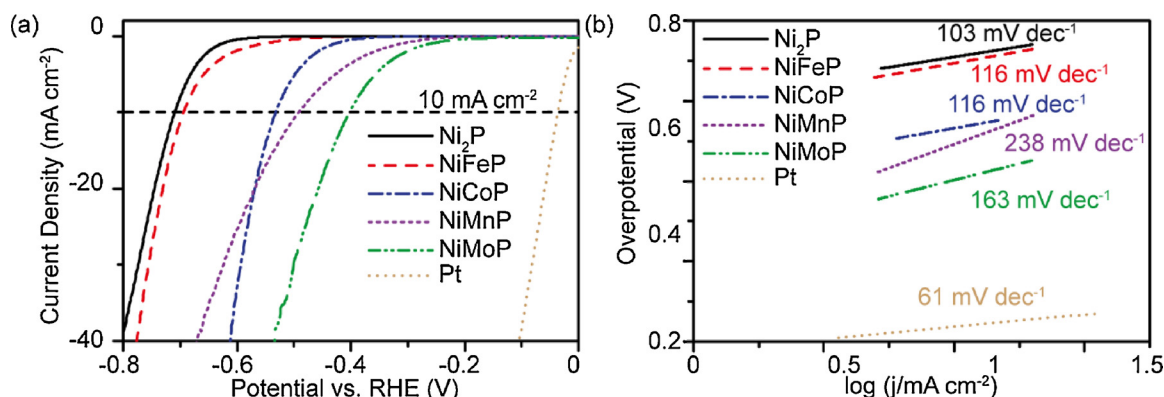

Fig. 3. (a) Linear sweep voltammograms and (b) Tafel plots of Ni_2P and various NiMP nanoparticles in 1 M KOH.

Table 2
Summary of electrochemical parameters of Ni_2P and various NiMP nanoparticles.

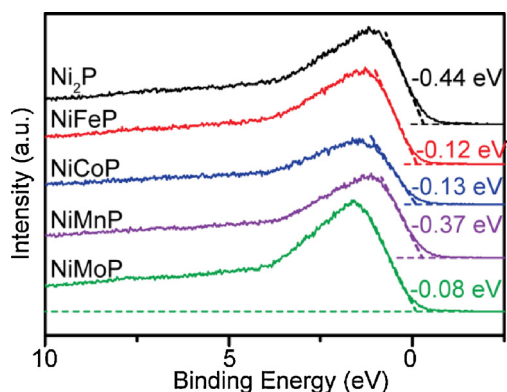|	Overpotential at 10 mA cm^{-2} (V)	Tafel Slope (mV dec^{-1})	Exchange Current Density (mA cm^{-2})
NiMoP	− 0.4	163	0.03
NiMnP	− 0.49	238	0.08
NiFeP	− 0.69	116	1×10^{-5}
NiCoP	− 0.53	116	2.5×10^{-4}
Ni_2P	− 0.71	103	1.3×10^{-6}

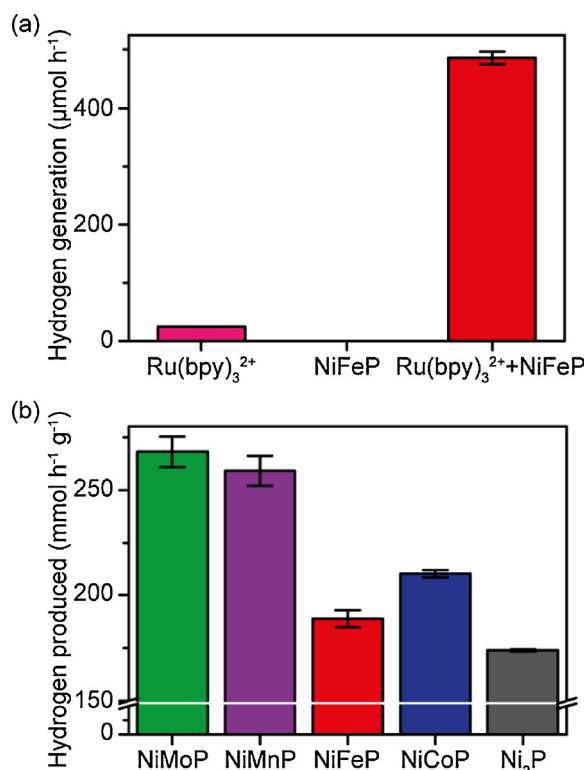**Fig. 4.** VB-XPS spectra of various NiMP nanoparticles.

Fig. 5. (a) Comparison of the amount of H_2 generated on an hourly basis in the presence of $[Ru(bpy)_3](ClO_4)_2$ only, NiFeP only, and both $[Ru(bpy)_3](ClO_4)_2$/NiFeP. (b) Photocatalytic activity of pristine and various NiMP nanoparticles are compared on an hourly basis per mass of phosphide-based catalyst. (DMF solvent is used).

tris(2,2′-bipyridyl)ruthenium(II) perchlorate $(Ru(bpy)_3(ClO_4)_2)$, which has a strong characteristic absorption in visible region (455 nm) with a high extinction coefficient [33]. Upon illumination, photo-generated electrons from this photosensitizer could be injected into the metallic

bands of NiMP for the proton reduction. The rapid electron transfer could also reduce the re-combination of photo-generated electrons and holes from the sensitizer to heat [34]. In addition to photosensitizer, triethanolamine was added as a sacrificial agent, which assists the re-generation of photosensitizer to ground state. The irradiation of NiFeP nanoparticles in the presence of $[Ru(bpy)_3](ClO_4)_2$ in $N,N′$-dimethylformamide (DMF) using 450 W solar simulator with air mass 1.5 filter for one hour resulted in the formation of 486 μmol of H_2. As far as we are aware, this photocatalytic HER activity is amongst the best reported in the literature (**Table S3**). In the two control experiments conducted under the same experimental conditions, only small amount of H_2 (24 μmol) was detected with the presence of $[Ru(bpy)_3](ClO_4)_2$ only, while no H_2 was detected with NiFeP nanoparticle only (Fig. 5a). These results confirm that NiFeP nanoparticle alone cannot carry out the photocatalytic HER, but they can catalyze the HER with excellent reactivity with the assistance of a light absorber, $[Ru(bpy)_3](ClO_4)_2$. It demonstrates that the excitons generated in $[Ru(bpy)_3](ClO_4)_2$ are effectively transferred to NiFeP nanoparticle, where they are used to catalyze the HER.

After assuring the synergetic effect between ruthenium complex and NiFeP nanoparticle, the reactivities of other NiMP nanoparticles were also studied (Fig. 5b). In general, metal doping in nickel phosphide nanoparticles shows a positive effect on the performance in dye-sensitized photocatalytic HER. The Ni_2P nanoparticle produces H_2 at a rate of 174 mmol h^{-1} g^{-1}, while NiFeP, NiCoP, NiMnP, and NiMoP all show a higher hydrogen production rate of 189, 210, 259, and 268 mmol h^{-1} g^{-1}, respectively. The rank of photocatalytic activity is as follows: $Ni_2P <$ NiFeP $<$ NiCoP $<$ NiMnP $<$ NiMoP.

Notice that the order of photocatalytic activity of different NiMP nanoparticles is identical to the decreasing order of overpotential for electrochemical hydrogen evolution. Such identical trend in HER catalytic activity is attributed to the same nature of active site on metal catalyst surface for H_2 production. Clearly, NiMP nanoparticles in dye-sensitized photocatalytic system act as the reaction center for hydrogen production upon receiving electrons from the excited dye. In order to further investigate the effect of metal doping on photocatalytic HER rate, the nickel-to-cobalt precursor ratio has been systematically varied from 3:1 to 1:2 during the synthesis of NiCoP nanoparticles. XRD, TEM images, elemental composition of NiCoP nanoparticles prepared under different nickel-to-cobalt ratio are shown in Supplementary Information (Figs. 6, S14 and **Table S2**). Their corresponding hydrogen production rates were measured and are shown in Fig. 7. A volcano-type activity relationship with respect to the Ni:Co precursor ratio can be seen, where the optimal value lies on the 1:1 ratio (the highest H_2 production rate of 209 mmol h^{-1} g^{-1}). Lowering cobalt content leads to a decrease in H_2 producing ability. As seen, Ni:Co ratios of 2:1 and 3:1 (abbreviated as NiCoP21 and NiCoP31) show the H_2 production rate of 180 and 147 mmol h^{-1} g^{-1}, respectively. On the other hand, increasing the Co contents beyond the optimal value to 1:2 Ni:Co ratio (NiCoP12) give a H_2 production rate of 140 mmol h^{-1} g^{-1}. It is thought that H_2 production rate is related to the delicate degree of electron filling of metallic bands as discussed with keeping the same NiMP hcp structure. Apparently, NiCoP11 with 1:1 Co substitution to Ni shows the optimal d-electron filling for the highest H_2 production rate.

Stability test was carried out with NiMoP nanoparticle in Ru$(bpy)_3^{2+}$-sensitized photocatalytic system (Fig. 8). The test was done in five separate runs of 5 h for the total duration of 25 h. After each run, NiMoP nanoparticle was isolated and photosensitizer and sacrificial agent were recharged. NiMoP nanoparticle clearly shows a good stability during the photocatalytic HER. The total photogenerated hydrogen quantities from the first and fifth runs are within 80% over 25 h despite a small loss in sample during the retests. Also, we confirmed that the morphology, crystal structure, and composition of NiMoP nanoparticle are retained without significant change after the photocatalysis from the post-HER characterizations (**Fig. S15**).

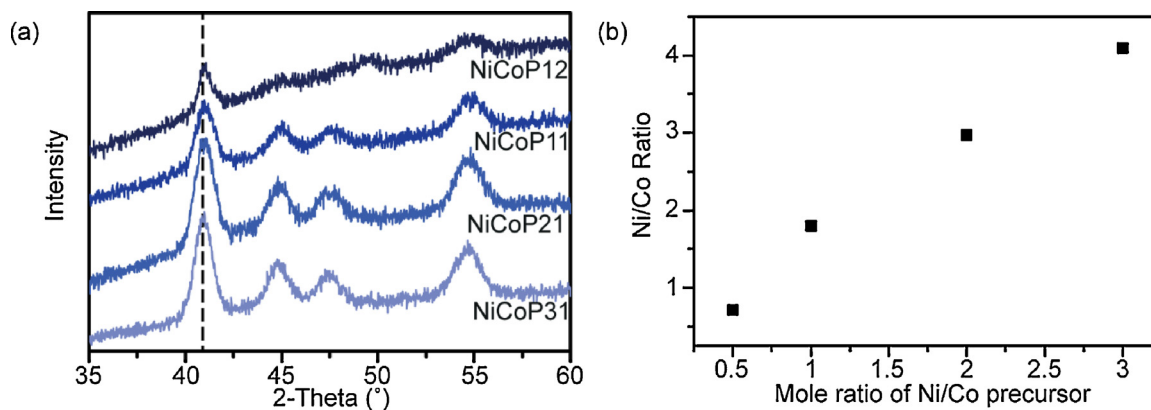Due to poor solubility of Ru$(bpy)_3^{2+}$ photosensitizer in water, the

Fig. 6. (a) XRD pattern of various NiCoP nanoparticles prepared using different Ni:Co precursor ratios and (b) relationship of elemental ratio between actual and loading nickel-to-cobalt ratios.
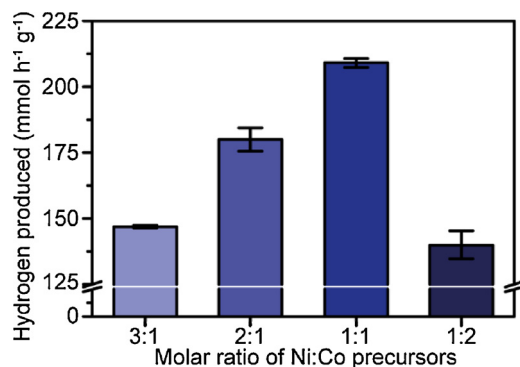

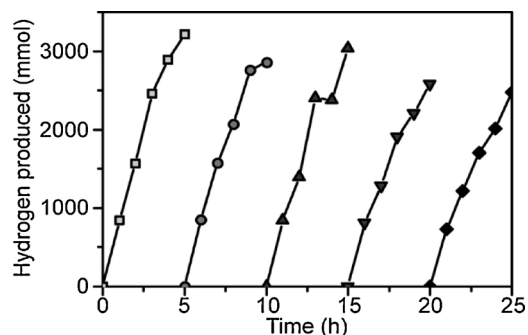**Fig. 7.** Effect of molar ratio of Ni:Co precursors on hydrogen production.

Fig. 8. Stability test on NiMoP nanoparticle in $Ru(bpy)_3^{2+}$-sensitized photocatalytic HER. Photocatalysis was carried out for 25 h as 5 separate runs with $Ru(bpy)_3^{2+}$ and sacrificial agent refurnished for each run.
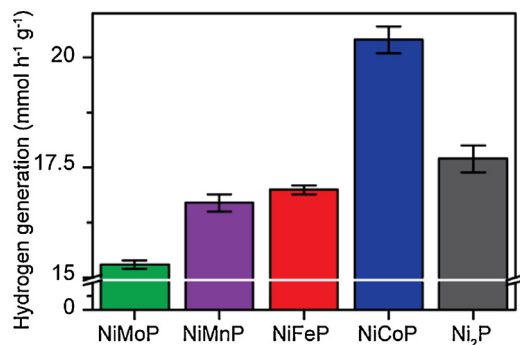

Fig. 9. Photocatalytic HER performance of pristine Ni_2P and various NiMP nanoparticles using eosin Y as the photosensitizer in H_2O.

photocatalytic HER activities of NiMP nanoparticles were acquired in DMF. Attempts to collect HER activities in water were also carried out using water-soluble eosin Y photosensitizer, the dye also with a characteristic absorption in visible region (**Fig. S16**). The conjugate base of eosin Y renders its high solubility in water. The NiMP nanoparticles were tested as HER photocatalysts in water and the results are summarized in Fig. 9. The HER activities between samples do not seem to deviate much, ranging from 15.3 mmol $h^{-1}g^{-1}$ for NiMoP nanoparticle, 16.7 mmol $h^{-1}g^{-1}$ for NiMnP nanoparticle, 17 mmol $h^{-1}g^{-1}$ for NiFeP nanoparticle, 17.7 mmol $h^{-1}g^{-1}$ for Ni_2P nanoparticle, to 20.4 mmol $h^{-1}g^{-1}$ for NiCoP nanoparticle. The low activities may reflect the poor electron transfer of eosin Y compared to the Ru complex but this system offers one of the highest reported photocatalytic HER activities in water compared to literature (**Table S4**). It is however, interesting to note that this order of catalytic activity in the presence of eosin Y is very different from that of $[Ru(bpy)_3](ClO_4)_2$. We attribute the main difference to the proton concentration that is much higher in water than in DMF. This will affect critically on the degree of hydrogen coverage on their surfaces. It has been shown that increasing hydrogen coverage can increase the Gibbs free energy of hydrogen adsorption (ΔG_H) [35,36].

To verify this point, a free energy (ΔG) calculation on the HER on the NiP structure was first modelled (**Fig. S17**) and the result is shown in Fig. 10 with different H coverage values. In these ΔG calculations, the total energy calculation was carried out by DFT method and the H atom was placed on the Ni site of the pristine NiP surface. Fig. 10a shows that the dramatic H coverage effect on HER efficiency of the pristine NiP surface lattice. By comparing 1/8 monolayer (ML) to 1/4 ML of H coverage values, the energy barrier for H chemisorption on NiP appears to increase by more than double than the original value. It is thought that the higher H-coverage on NiP inhibits further absorption of H, resulting in the overall lowering of the HER efficiency. We further consider the contribution of various transition metal dopants (Fe, Co, Mn, and Mo) at 1/4 and then 1/8 ML H coverages (Fig. 10b and c). The doping that we modelled was based on the substitution of Ni by M (M = Fe, Co, Mn, and Mo). As seen from the two figures, their ΔG values are highly dependent on the degree of H coverage [19,37]. As previously discussed on the 'volcano relationship' by Nørskov and co-workers [19], the ΔG value closer to the thermoneutral line (0 eV) whereby the thermodynamic H^+ reduction to H_2 production is reached, gives higher HER efficiency. Since larger positive ΔG value represents too weak H adsorption (disfavour for Volmer step but favour for Tafel step) while larger negative ΔG denotes too strong H-adsorption (favour for Volmer step but disfavour for Tafel step), the ΔG value near 0 eV therefore suggests the optimal HER performance.

In a higher H coverage (Fig. 10b) on the NiMP surface, the H absorption energy profile on NiCoP surface clearly gives the best HER
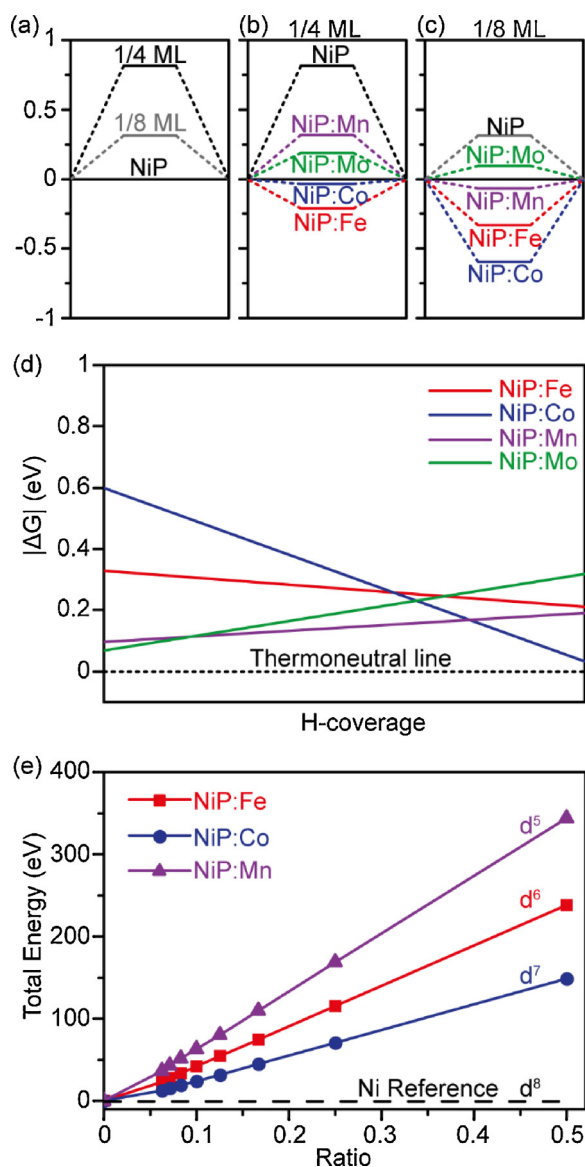
Fig. 10. (a) Free energy for H absorption on pristine NiP with different H coverage. Comparison of ΔG for the H absorption on pristine NiP and NiMP surface systems at the coverage of (b) 1/4 ML and (c) 1/8 ML (M = Fe, Co, Mn, and Mo). (d) Free energy trend compared to the thermoneutral line for pristine NiP and NiMP surface systems. (e) Total energy trend with related to the doping level in NiMP surface systems.

changes depending on the H-coverage. On the other hand, the pristine NiP, NiMnP and NiMoP surfaces all exhibit positive slope at increasing H coverage, which would lower the HER activities.

Based on these DFT calculations, we conclude that NiMoP gives superior HER rate at the low H coverage. This is consistent with our observations that this catalyst surface gives highest HER performance in electrochemical and photocatalytic activation at low H coverage. On the other hand, NiCoP gives the highest HER photocatalytic activity at high H coverage when aqueous eosin Y photosensitizer is used. Thus, we demonstrate the highly tunable activities of these single-phase composites dependent on the electron filling of their metallic bands and H-coverage. We also compared the total energy in a physicochemical trend (Fig. 10e). It is found that the NiCoP gives more stable configuration than the other NiMP systems.

5. Conclusions

In this work, we show that various transition metal dopers, including cobalt, iron, manganese, and molybdenum are successfully added into the nickel phosphide crystal lattice as a single phase without significant structural change. The EXAFS data indicates that the typical Fe gives the same neighboring local bonding with Ni and P, implying the successful substitution of Ni in nanoparticle level. The as-synthesized metal-doped nickel phosphide nanoparticles are semi-mono-dispersed spherical in shape and possessing the same hexagonal crystal structure as Ni_2P at this high level of doping. The metal-doped and pristine nickel phosphide nanoparticles are shown to maintain the same metallic properties as Ni_2P, which is crucially important as electrode material without introducing impedance to the system. Also, in this study, the rational and tunable properties of nickel phosphide nanoparticles substituted with various metal dopants in both electro- and photochemical HER are clearly demonstrated. *For example*, Ni (d^8) contains more than sufficient electrons in its d-band which leads to a poor HER activity. The rational substitution of Ni by transition metals of lower numbers of d electrons could render the doped nickel phosphide nanoparticles more active than that of pristine nickel phosphide nanoparticle due to the optimal electron filling. Similarly, the extent of Ni substitution by Co can also allow the fine tuning of the electron filling to the metallic bands of NiCoP. Molybdenum-doped nickel phosphide nanoparticle is found to have the lowest overpotential of 0.4 V *vs.* RHE and a Tafel slope of 163 mV dec^{-1} in alkaline medium, which is identified as a promising candidate among the various doped samples for the replacement of Pt based catalysts. Also, metal-doped nickel phosphide nanoparticles show promising activity in the dye-sensitized photocatalytic hydrogen evolution reaction. Again, molybdenum-doped nickel phosphide nanoparticle shows the best activity on hydrogen production with a rate of 268 mmol h^{-1} g^{-1} in the presence of $[Ru(bpy)_3](ClO_4)_2$ in DMF. On the other hand, cobalt-doped nickel phosphide nanoparticle exhibits the best hydrogen production rate of 20.4 mmol h^{-1} g^{-1} in eosin Y-sensitized photocatalytic system in water. We attribute the difference in HER activity to the different degree of H coverage especially in the case for Co, which can also be the key factor of influencing the HER activity exerted by the environment.

Overall, it is demonstrated the Ni sites on Ni_2P can be substituted by other transition metals at high doping level, to yield the single phase NiMP solid structure, which displays tunable catalytic properties for HER. This class of materials is a promising candidate to replace Pt used in optical cells for hydrogen production.

Acknowledgement

performance as it gives only -0.03 eV. This can explain the fact that the use of water with higher proton concentration (eosin Y) renders this catalyst the most active for HER compared to the other (see Fig. 9). However, the NiFeP surface does not favour for H$^+$ adsorption and reduction while both NiMoP and NiMnP systems are energetically unfavourable for HER. In contrast, in a lower H coverage (Fig. 10c), as our case using ruthenium complex in DMF, both NiMoP and NiMnP become energetically favourable for higher HER activity, whereas for the NiCoP system, the ΔG is far from zero value. Under this situation, the H desorption may be inhibited due to too strong M−H bonding.

Fig. 10d illustrates the changes of free energy with H coverage for pristine NiP and NiMP surfaces, with respect to the thermoneutral line. Both Co and Fe insertion improve their HER activities at higher H coverage, while in the case of Fe, it varies much more gently with the H coverage. This indicates that NiFeP gives good HER performance only under an extremely high H coverage. But NiCoP is much sensitive to the H coverage value. It is noteworthy that their relative HER performance

Appendix A. Supplementary data

Supplementary material related to this article can be found, in the online version, at doi:https://doi.org/10.1016/j.apcatb.2018.09.103.

References

[1] T.S. Teets, D.G. Nocera, Chem. Commun. (Camb.) 47 (2011) 9268.
[2] F. Wang, W.G. Wang, H.Y. Wang, G. Si, C.H. Tung, L.Z. Wu, ACS Catal. 2 (2012) 407.
[3] S.M. Arachchige, K.J. Brewer, Energy Production and Storage: Inorganic Chemical Strategies for a Warming World, John Wiley & Sons, Chichester, West Sussex, UK, 2010.
[4] C.G. Morales-Guio, L.A. Stern, X. Hu, Chem. Soc. Rev. 43 (2014) 6555.
[5] E. Aharon-Shalom, A. Heller, J. Electrochem. Soc. 129 (1982) 2865.
[6] A. Fujishima, K. Honda, Nature 238 (1972) 37.
[7] Y. Li, H. Wang, L. Xie, Y. Liang, G. Hong, H. Dai, J. Am. Chem. Soc. 133 (2011) 7296.
[8] P. Liu, J.A. Rodriguez, J. Am. Chem. Soc. 127 (2005) 14871.
[9] E.J. Popczun, J.R. McKone, C.G. Read, A.J. Biacchi, A.M. Wiltrout, N.S. Lewis, R.E. Schaak, J. Am. Chem. Soc. 135 (2013) 9267.
[10] Z. Huang, Z. Chen, Z. Chen, C. Lv, H. Meng, C. Zhang, ACS Nano 8 (2014) 8121.
[11] M. Ledendecker, S.K. Calderón, C. Papp, H.-P. Steinruck, M. Antonietti, M. Shalom, Angew. Chem. Int. Ed. 54 (2015) 12361.
[12] Y. Pan, Y. Liu, J. Zhao, K. Yang, J. Liang, D. Liu, W. Hu, D. Liu, Y. Liu, C. Liu, J. Mater. Chem. A 3 (2015) 1656.
[13] Y. Pan, W.H. Hu, D.P. Liu, Y.Q. Liu, C.G. Liu, J. Mater. Chem. A 3 (2015) 13087.
[14] Y. Bai, H. Zhang, X. Li, L. Liu, H. Xu, H. Qiu, Y. Wang, Nanoscale 7 (2015) 1446.
[15] A. Han, S. Jin, H.L. Chen, H.X. Ji, Z.J. Sun, P.W. Du, J. Mater. Chem. A 3 (2015) 1941.
[16] D. Zeng, W. Xu, W.-J. Ong, J. Xu, H. Ren, Y. Chen, H. Zheng, D.-L. Peng, Appl. Catal. B 221 (2018) 47.
[17] Z. Sun, H. Zheng, J. Li, P. Du, Energy Environ. Sci. 8 (2015) 2668.
[18] S. Cao, Y. Chen, C.-J. Wang, P. He, W.-F. Fu, Chem. Commun. (Camb.) 50 (2014) 10427.
[19] J.K. Nørskov, T. Bligaard, A. Logadottir, J.R. Kitchin, J.G. Chen, S. Pandelov, U. Stimming, J. Electrochem. Soc. 152 (2005) J23.
[20] J. Kibsgaard, C. Tsai, K. Chan, J.D. Benck, J.K. Nørskov, F. Abild-Pedersen, T.F. Jaramillo, Energy Environ. Sci. 8 (2015) 3022.
[21] J. Greeley, T.F. Jaramillo, J. Bonde, I. Chorkendorff, J.K. Nørskov, Nat. Mater. 5 (2006) 909.
[22] Y. Li, P. Hasin, Y. Wu, Adv. Mater. 22 (2010) 1926.
[23] Y. Yang, H. Fei, G. Ruan, C. Xiang, J.M. Tour, ACS Nano 8 (2014) 9518.
[24] S. Chen, S.-Z. Qiao, ACS Nano 7 (2013) 10190.
[25] C. Zhang, Y. Xie, H. Deng, C. Zhang, J.-W. Su, Y. Dong, J. Lin, Int. J. Hydrogen Energy 43 (2018) 7299.
[26] J. Li, M. Yan, X. Zhou, Z.-Q. Huang, Z. Xia, C.-R. Chang, Y. Ma, Y. Qu, Adv. Funct. Mater. 26 (2016) 6785.
[27] Y. Li, J. Liu, C. Chen, X. Zhang, J. Chen, ACS Appl. Mater. Interfaces 9 (2017) 5982.
[28] L. Bi, X. Gao, L. Zhang, D. Wang, X. Zou, T. Xie, ChemSusChem 11 (2018) 276.
[29] F. Lyu, Y. Bai, Q. Wang, L. Wang, X. Zhang, Y. Yin, Dalton Trans. 46 (2017) 10545.
[30] H.-R. Seo, K.-S. Cho, S.-H. Kim, Y.-K. Lee, J. Korean Phys. Soc. 56 (2010) 2083.
[31] M.M. Jaksic, Int. J. Hydrogen Energy 26 (2001) 559.
[32] E. Navarro-Flores, Z. Chong, S. Omanovic, J. Mol. Catal. A Chem. 226 (2005) 179.
[33] J. Willkomm, K.L. Orchard, A. Reynal, E. Pastor, J.R. Durrant, E. Reisner, Chem. Soc. Rev. 45 (2016) 9.
[34] C. Tsai, K. Chan, J.K. Nørskov, F. Abild-Pedersen, Surf. Sci. 640 (2015) 133.
[35] X. Fan, S. Wang, Y. An, W. Lau, J. Phys. Chem. C 120 (2016) 1623.
[36] J. Durst, A. Siebel, C. Simon, F. Hasche, J. Herranz, H.A. Gasteiger, Energy Environ. Sci. 7 (2014) 2255.
[37] K. Kalyanasundaram, Coord. Chem. Rev. 46 (1982) 159.